Hyperelastic, Robust, Fire-Safe Multifunctional MXene Aerogels with Unprecedented Electromagnetic Interference Shielding Efficiency

Hengrui Wang, Yue Jiang, Zhewen Ma, Yongqian Shi,* Yanjun Zhu, Ruizhe Huang, Yuezhan Feng, Zubin Wang, Min Hong, Jiefeng Gao, Long-Cheng Tang, and Pingan Song*

MXene aerogels have shown great potential for many important functional applications, in particular electromagnetic interference (EMI) shielding. However, it has been a grand challenge to create mechanically hyperelastic, air-stable, and durable MXene aerogels for enabling effective EMI protection at low concentrations due to the difficulties in achieving tailorable porous structures, excellent mechanical elasticity, and desired antioxidation capabilities of MXene in air. Here, a facile strategy for fabricating MXene composite aerogels by co-assembling MXene and cellulose nanofibers during freeze-drying followed by surface encapsulation with fire-retardant thermoplastic polyurethane (TPU) is reported. Because of the maximum utilization of pore structures of MXene, and conductive loss enhanced by multiple internal reflections, as-prepared aerogel with 3.14 wt% of MXene exhibits an exceptionally high EMI shielding effectiveness of 93.5 dB, and an ultra-high MXene utilization efficiency of 2977.71 dB g g^{-1}, tripling the values in previous works. Owing to the presence of multiple hydrogen bonding and the TPU elastomer, the aerogel exhibits a hyperelastic feature with additional strength, excellent stability, superior durability, and high fire safety. This study provides a facile strategy for creating multifunctional aerogels with great potential for applications in EMI protection, wearable devices, thermal management, pressure sensing, and intelligent fire monitoring.

1. Introduction

MXene, as a recently emerging 2D inorganic material, typically represented by Ti$_3$C$_2$T$_x$ (T$_x$ represents a general surface termination, such as O, F, or OH groups), has attracted great attention because of its metal-like electrical conductivity, tunable hydrophilic surface, and high mechanical properties.[1] These unique merits make MXene show great application potential in the areas of electromagnetic interference (EMI) shielding,[2] flame retardants,[3] electrical sensors,[4] etc. However, large aspect ratios and high specific surface areas render 2D lamellar MXene tend to form agglomeration, thus limiting its EMI efficiency and other functions, in addition to its ease of oxidation in moist air.[5]

Constructing MXene aerogels represents an efficient strategy to achieve high EMI efficiency and multifunction (e.g., thermal insulation, and sensing).[1b] Compared with MXene films, MXene aerogels often show higher EMI shielding effectiveness (SE)

H. Wang, Y. Shi, Y. Zhu, R. Huang
College of Environment and Safety Engineering
Fuzhou University
2 Xueyuan Road, Fuzhou 350116, China
E-mail: shiyq1986@fzu.edu.cn
Y. Jiang
China-Australia Institute for Advanced Materials and Manufacturing
Jiaxing University
Jiaxing 314001, China

Z. Ma
Department of Inorganic Materials
School of Materials Science and Engineering
Tongji University
Shanghai 201804, China
Y. Feng
Key Laboratory of Materials Processing and Mold Ministry of Education
National Engineering Research Center for Advanced Polymer Processing
Technology
Zhengzhou University
Zhengzhou 450002, China
Z. Wang
Institute of Safety Science and Engineering
School of Mechanical and Automotive Engineering
South China University of Technology
Wushan Road 381, Guangzhou 510641, China

**ADVANCED
SCIENCE NEWS**

www.advancedsciencenews.com

**ADVANCED
FUNCTIONAL
MATERIALS**

www.afm-journal.de

whether they have an either aligned lamellar architecture[6] or foam-like structure.[7] This is because the hierarchical pores in aerogels can facilitate multiple reflections of incident electromagnetic waves (EMWs), besides the high electrical conductivity of MXene. To further boost the EMI shielding and mechanical properties, some functional fillers, such as graphene,[8] porous carbon,[9] and carbon nanotubes,[10] are added to create MXene composite aerogels because of their synergistic effects. Moreover, low-density 3D MXene-based aerogels usually exhibit high adsorption efficiency and good thermal insulation properties besides their great application potential for piezoresistive sensing,[11] thermal energy conversion,[12] salt deposition,[13] and stable anode for foldable batteries[14] because of their porous structures, high electrical conductivity, and thermoelectric features. Therefore, the creation of mechanically robust, air-insensitive, multifunctional MXene aerogels with high EMI SE will help expedite their practical applications in the field of electromagnetic protection.[15]

Currently, component concoction and microstructure design are two promising approaches for the fabrication of high-performance MXene aerogels for effective EMI shielding.[16] The presence of heterogeneous dielectric/magnetic components can introduce additional loss mechanisms, including dielectric, magnetic, and conductive loss, thus directly contributing to the EMI SE of the final aerogels. For instance, the addition of MXene/nickel ferrite components leads to an enhanced EMI shielding performance by improving impedance matching, moderate magnetic loss, and multiple interfaces, causing more dissipation of incident EMWs.[17] Additionally, MXene hybridized with high electrically conductive Ag nanowires[18] and poly(3,4-ethylenedioxythiophene):poly(styrene sulfonate) (PEDOT:PSS)[19] can result in higher ohmic loss and accumulate heterogeneous interface charges to enhance polarization loss.

Despite great advances in MXene aerogels for EMI shielding, it remains a great challenge to create hyperelastic, mechanically robust, durable multifunctional MXene aerogels for efficient EMI shielding with a very low content of expensive MXene nanosheets. Regarding EMI efficiency, the construction of continuous inner networks in MXene aerogels represents an effective method to prepare highly efficient EMI shielding materials at a low loading level of MXene because of the high utilization efficiency.[1b,20] With respect to the elasticity (shape recoverability) and the mechanical property of MXene aerogels, they are directly dependent on the interfacial interactions and cross-linking of MXene nanosheets. Although the surfaces of MXene nanosheets have rich hydroxyl groups capable of forming hydrogen bonding, pure MXene aerogels show poor elasticity and mechanical properties. Therefore, some polymers are usually used as binders for MXene sheets to improve their mechanical properties.[15,21] The hydrophilic polymer binders can form strong hydrogen bonding with MXene and thus avoid the aggregation of the latter, leading to improved mechanical properties. For instance, polyvinyl alcohol (PVA)[22] and cellulose[23] were used to create MXene composite aerogels via freeze-drying, and the resultant composite aerogels show higher mechanical performances in comparison to both pure MXene and polymer aerogels because of effective stress transfer. In addition, the significantly mismatched conductivity in the MXene/polymer interface can generate strong interfacial polarization under the electric field, thereby promoting electromagnetic energy loss and enhancing electromagnetic protection.[24]

The durability of MXene aerogels is a key factor for their practical EMI shielding applications. Because MXene sheets are highly oxygen sensitive and tend to degrade when exposed to a humid air environment, MXene aerogels are more susceptible to oxidation due to their higher specific area. As a result, the electrical conductivity of MXene degrades, and thus its EMI and other physical properties inevitably undergo deterioration.[25] To delay or prevent the oxidation process, a facile approach is to isolate MXene from the air,[26] such as storing MXene aqueous suspensions under argon[27] or dispersing MXene in organic solvents (e.g., acetone, acetonitrile, and isopropanol).[28] Also, loading antioxidants, including polyanionic salts and sodium L-ascorbate, onto the MXene surface can significantly retard the oxidation.[29] However, these methods are not suitable for MXene-based aerogels.

This work aims to create mechanically hyperelastic and robust, air-stable, and durable multifunctional MXene aerogels for efficient EMI shielding at a very low concentration of MXene. To this end, multifunctional MXene composite aerogels were prepared by co-assembling $Ti_3C_2T_x$ MXene and cellulose nanofibers (CNF) via freeze-drying followed by surface encapsulation using silicon microencapsulated ammonium polyphosphate (SiAPP) filled hydrophobic thermoplastic polyurethane (TPU). As-designed CNF-MXene aerogels show a porous architecture because of the presence of 1D CNF. The lightweight MXene composite aerogel (with a density of 0.26 g cm^{-3}) achieves a very high EMI SE (93.5 dB in X-band) at an ultralow MXene loading of 3.14 wt%, and a record-high EMI utilization efficiency of 2977.71 dB g g^{-1}. TPU/SiAPP acts as a fire-retardant and elastic binder to enhance the mechanical and fire-retardant properties of the resultant composite aerogels and serves as an antioxidative coating to improve their air stability. The as-created multifunctional MXene composite aerogels hold great potential for applications in the field of defense, aerospace, and smart wearable electronics.

M. Hong, P. Song
Centre for Future Materials
University of Southern Queensland
Springfield 4300, Australia
E-mail: pingan.song@usq.edu.au

J. Gao
School of Chemistry and Chemical Engineering
Yangzhou University
Yangzhou 225002, China

L.-C. Tang
Key Laboratory of Organosilicon Chemistry and Material
Technology of MoE
College of Material, Chemistry and Chemical Engineering
Hangzhou Normal University
Hangzhou 311121, China

P. Song
School of Agriculture and Environmental Science
University of Southern Queensland
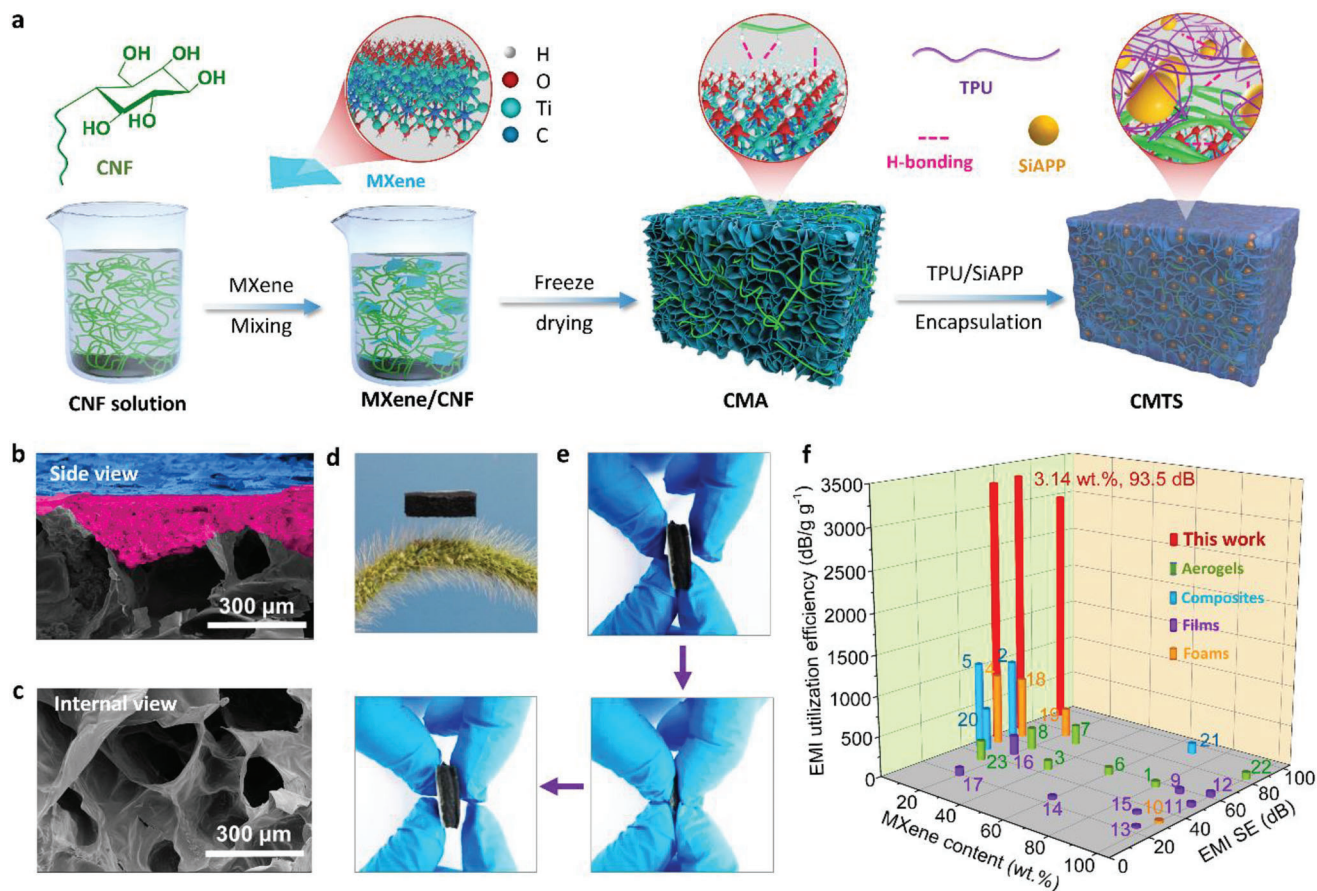Springfield 4300, Australia

ADVANCED
SCIENCE NEWS
www.advancedsciencenews.com

ADVANCED
FUNCTIONAL
MATERIALS
www.afm-journal.de

Figure 1. Preparation and characterization of CNF-MXene composite aerogels (CMTS). a) Schematic illustration for the preparation of CMTS. SEM images of the CMTS: b) side view and c) internal view. d) Digital photo of $CM_{19}TS_{20}$ standing in the weeds. e) Compression recovery of $CM_{19}TS_{20}$. f) Comparison of the EMI utilization efficiency of MXene and EMI SE as a function of MXene content of as-prepared MXene-based aerogel with those reported in the literature.

2. Results and Discussion

Figure 1a schematically illustrates the fabrication process of CNF-MXene aerogel (CMA) functionally encapsulated by the TPU/SiAPP using a combined freeze-drying and surface encapsulation approach. Specifically, $Ti_3C_2T_x$ MXene nanosheets were firstly synthesized by etching Ti_3AlC_2 with LiF and HCl according to the reference-outlined method.[30] As-prepared MXene nanosheets were further characterized by X-ray diffraction (Figure S1a, Supporting Information),[31] scanning electron microscopy (SEM) (Figure S1b,c, Supporting Information), transmission electron microscopy (TEM) (Figure S1d, Supporting Information) and atomic force microscopy (AFM) (Figure S1e,f, Supporting Information). The thickness of MXene nanosheets, as determined by AFM, is ≈1.07–1.21 nm. Upon direct freeze-drying, the MXene flakes and CNFs self-assembled to form CNF-MXene (CMA) aerogels, owing to the strong hydrogen bonding interaction between the abundant hydrophilic functional groups on their surface. To endow aerogels with desired mechanical elasticity and robustness as well as oxygen resistance, CMAs were subsequently encapsulated with flame retardant TPU/SiAPP mixture. The resultant composite aerogels were denoted as CM_xTS_y, where M_x and T_y represented the concentra-

tion of MXene (mg g^{-1}), and the mass fraction of SiAPP in the TPU/SiAPP mixture, respectively.

$CM_{19}TS_{20}$ exhibits a heterogeneous porous structure ranging from 10 to 100 μm in size (Figure 1b,c). Despite being encapsulated with the TPU/SiAPP, the $CM_{19}TS_{20}$ still shows a very low density of 0.26 g cm^{-3} and thus can be effortlessly supported by bristlegrass (Figure 1d). The composite aerogel exhibits outstanding compressive resilience, maintaining its thickness even after multiple compression cycles (Figure 1e; Movie S1, Supporting Information). As-prepared $CM_{19}TS_{20}$ only containing 3.14 wt% of MXene shows an EMI SE as high as 93.5 dB. As a result, if the MXene utilization efficiency is defined by the EMI SE divided by the mass percentage of conductive fillers (dB g g^{-1}), our MXene aerogel reaches a record utilization efficiency up to 2977.71 dB g^{-1}, which is over threefold of the highest value in literature (Figure 1f). Such an unprecedented EMI shielding efficiency can greatly expedite the practical application of MXene in industrial settings due to the significantly reduced use cost.

Freeze-drying processing is an efficient route to construct lightweight porous structures.[11,32] As-developed CMA aerogel has an uneven and irregular porous structure with a size ranging from several hundred micrometers to several millimeters, as reflected by cross-sectional SEM images (**Figure 2**a–d). With an
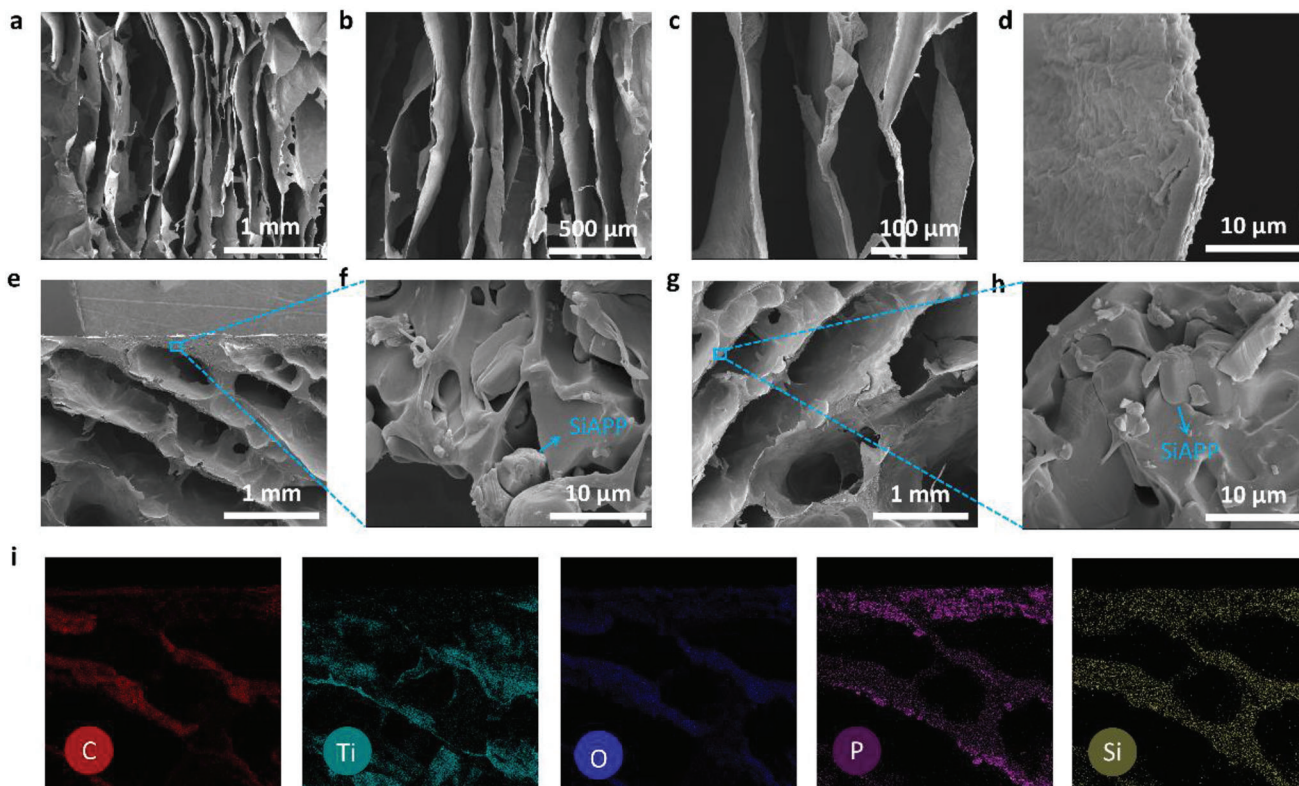
**ADVANCED
SCIENCE NEWS**

www.advancedsciencenews.com

**ADVANCED
FUNCTIONAL
MATERIALS**

www.afm-journal.de

Figure 2. Structural characterization of CNF-MXene composite aerogels (CMTS). a–d) Cross-section SEM images of $CM_{19}A$. e–h) Cross-section SEM images of $CM_{19}TS_{20}$. i) EDS mapping images of different elements for $CM_{19}TS_{20}$.

increase in MXene concentration, a channel structure is formed, and pores in the aerogel become smaller to a certain extent (Figure S2a,b, Supporting Information). The large and discontinuous channels in the CMA not only facilitate the penetration of polymer monomers or solutions into the aerogel for further functionalization, but also reduce capillary forces to prevent aerogel contraction. Interestingly, although both pure MXene aerogel (MA) and cellulose aerogel (CA) have continuous 3D porous structures (Figure S3, Supporting Information), they cannot maintain the original morphology when being immersed in the solution, making them impossible to be encapsulated by TPU, even for the CMA sample (Figure S4, Supporting Information). This result is probably attributed to strong hydrogen bonding interactions formed by CNF embedded in MXene.

The XRD spectra (Figure S5a, Supporting Information) reveal the intercalation of CNF into MXene, resulting from the increased interlayer spacing of MXenes in the CMA. The peak assigned to (002) lattice plane of the CMA shifts to a lower angle, compared to that of the MA, suggesting successful intercalation of CNF into the interlayer of MXene.[33] The strengthened interconnection within MXene flakes originates from the CNF binders, which provide hydrogen bonding with the MXene flakes. This physical hydrogen-bond cross-linking is further confirmed by Fourier-transform infrared (FTIR) spectra (Figure S5b, Supporting Information). It is easy to observe the weakened characteristic absorption peak of hydroxyl groups in the CMA at 3340 cm^{-1} and a 10 cm^{-1} redshift compared to that of CA. These results suggest that strong hydrogen bonding between MXene

and CNF is the driving force for intercalation, well agreeing with previous studies.[34] Therefore, the CMA can maintain its original thickness after multiple compression and rebound, demonstrating its robust mechanical elasticity (Movie S2, Supporting Information).

To enhance both the mechanical and flame retardant properties of CMA, it was impregnated into TPU/SiAPP dispersion to achieve surface encapsulation. The TPU/SiAPP was then cured on the CMA aerogels surface (Figure S6, Supporting Information) to create a rough surface that effectively prevents moisture from entering the aerogels and alleviates the oxidation of MXene. Flame-retardant TPU encapsulation makes the pore structure of CMA more uniform and smoother (Figure 2e,g). Increasing MXene contents in the aerogel leads to smaller and denser pores, as revealed by the SEM results of $CMTS_{20}$ (Figure S7a–d, Supporting Information). The cross-section SEM images indicate the successful penetration of flame retardant TPU into the skeleton of the aerogel (Figure 2f,h; Figure S7e–h, Supporting Information). According to energy-dispersive X-ray spectroscopy (EDS) mappings (Figure 2i), C, O, and Ti elements are distributed uniformly in the aerogel, while P and Si elements are only found to be rich in the skeleton and the aerogel surface, indicating the complete penetration of these polymer/composite materials are successfully assembled into the skeleton of aerogels and their surfaces (Figure S8, Supporting Information). These findings demonstrate the successful integration of TPU/SiAPP with CMA, which contributes to improved mechanical, flame retardant, and oxygen-resistant properties of the CMTS.
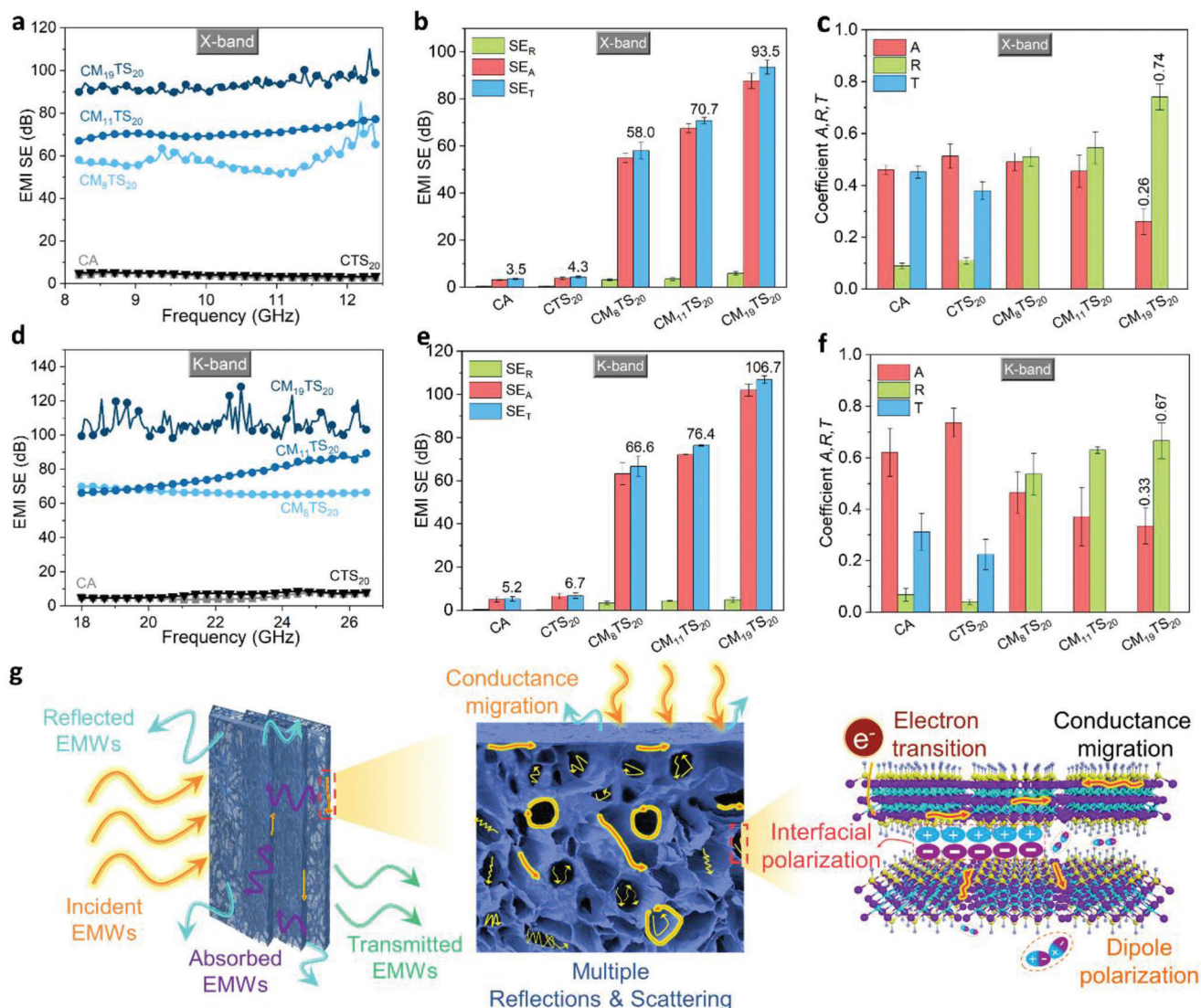
**ADVANCED
SCIENCE NEWS**

www.advancedsciencenews.com

**ADVANCED
FUNCTIONAL
MATERIALS**

www.afm-journal.de

Figure 3. Excellent EMI efficiency of CNF-MXene composite aerogels. a) The EMI SE curves of composite aerogels under the X-band. b) The SE_T, SE_A, and SE_R values of composite aerogels under the X-band. c) The shielding parameters A, R, and T of composite aerogels under the X-band. d) The EMI SE curves of composite aerogels under the K-band. e) The SE_T, SE_A, and SE_R values of composite aerogels under the K-band. f) The shielding parameters A, R, and T of composite aerogels under the K-band. g) The proposed EMI shielding mechanism.

The EMI shielding performances of the CM_xTS_{20} with different MXene concentrations in the X-band range (8.2–12.4 GHz) and the K-band range (18.0–26.5 GHz) are shown in **Figure 3**a,d, respectively. The EMI SE values of composite aerogels increase with improving MXene content. The average EMI SE values of the $CM_{19}TS_{20}$ are as high as 93.5 and 106.7 dB in X- and K-band, respectively, indicating that it is capable of blocking more than 99.99999997% of EMWs. Even at a low concentration of MXene, the CM_8TS_{20} still shows an average EMI SE of 66.6 dB in the K-band, which is much higher than the minimum standard of commercial application (20 dB).[35] To understand the shielding mechanism of EMWs incident into the interior of the composite aerogels, the total EMI SE (SE_T), reflection loss (SE_R), and absorption loss (SE_A) of all electrically conductive aerogel samples are plotted in Figure 3b,e. The values of SE_A for the aerogel samples are enhanced both in X- and K-band with increasing MXene loading, whereas the values of SE_R of the composite aerogels are maintained at a relatively low level, indicating an absorption-dominant EMI shielding mechanism. The presence of MXene introduces more absorption shielding, which is different from traditional conductive materials, such as metal or graphite.[36] The absorption shielding mechanism can effectively avoid secondary electromagnetic pollution caused by those conductive materials based on reflective shielding. A possible reason is that porous structures of MXene serve as resonators inside the material. The approximate hexagonal MXene micropore formed by ice crystals sublimation creates abundant internal reflections, resulting in more EMWs adsorption loss.

The normalized relationships between the reflection coefficient (R), absorption coefficient (A), and transmission coefficient

**ADVANCED
SCIENCE NEWS**

www.advancedsciencenews.com

**ADVANCED
FUNCTIONAL
MATERIALS**

www.afm-journal.de

Table 1. Comparison of EMI SE properties of MXene-based materials reported in the literature.

Materials	Filler type	Filler content [wt%]	EMI SE [dB]	EMI utilization efficiency [dB g g^{-1}]	Fire-retardant (Yes/no)	Reference
CNF/TS$_{20}$	Ti$_3$C$_2$T$_x$	1.76	58.0	3295.45	Yes	This work
CNF/TS$_{20}$	Ti$_3$C$_2$T$_x$	2.13	71.0	3333.33	Yes	This work
CNF/TS$_{20}$	Ti$_3$C$_2$T$_x$	3.14	93.5	2977.71	Yes	This work
Epoxy	Ti$_3$C$_2$T$_x$-RGO	80	56.4	70.5	No	[8]
PS	Ti$_3$C$_2$T$_x$	6.2	62	1000	No	[37]
ANF	Ti$_3$C$_2$T$_x$	40	44.7	111.75	No	[38]
SA	Ti$_3$C$_2$T$_x$	6.1	53.9	883.61	No	[39]
Epoxy	Ti$_3$C$_2$T$_x$	4.25	46	1082.35	No	[40]
CNF	APP/Ti$_3$C$_2$T$_x$	60	55	91.67	Yes	[41]
Wood	Ti$_3$C$_2$T$_x$	30	71.8	239.33	No	[4]
ANFs	Ti$_3$C$_2$T$_x$	21	56.8	270.48	No	[42]
SA	Ti$_3$C$_2$T$_x$	90	57	63.33	No	[43]
/	Ti$_3$C$_2$T$_x$	Bulk	32	32	No	[44]
/	Ti$_2$CT$_x$	Bulk	50	50	No	[45]
/	Ti$_3$CNT$_x$	Bulk	61.4	61.4	No	[25]
HEC	Ti$_3$C$_2$T$_x$	96.8	24	24.79	No	[46]
ANF	Ti$_3$C$_2$T$_x$	60	24.5	40.83	Yes	[47]
ANF	Ti$_3$C$_2$T$_x$	90	33.1	36.78	No	[48]
ANF	Ti$_3$C$_2$T$_x$/AgNW	20	48.1	240.5	No	[49]
PVDF	Ti$_3$C$_2$T$_x$/Ni	20	19.5	97.5	No	[50]
PCF	Ti$_3$C$_2$T$_x$	8.5	65	764.70	Yes	[51]
APU	Ti$_3$C$_2$T$_x$	21.1	76.2	361.14	No	[52]
PAA	Ti$_3$C$_2$T$_x$	8.5	45.3	532.94	No	[24a]
PP	Ti$_3$C$_2$T$_x$	70	92.1	131.57	Yes	[53]
/	RGO/Ti$_3$C$_2$T$_x$	Bulk	83.3	83.3	No	[54]
PEG	Ti$_3$C$_2$T$_x$/RGO	14.7	36	244.90	No	[55]

(T) were calculated to further evaluate the surface EMI shielding mechanism for the above samples (Figure 3c,f). With the merging of the MXene component, the T value of the composite aerogels is close to 0, indicating a superior EMI shielding ability. Compared to the CA, the composite aerogels filled with MXene present a higher R-value, mainly attributed to the interface reflections caused by the high conductive MXene in the aerogel skeleton. With the increased loading of MXene, the R values for composite aerogels exhibited a slight improvement in both X- and K-band, which are 0.74 and 0.67, respectively. The increase of MXene aerogel SE$_R$ also confirms the enhancement of MXene reflection shielding in Figure 3b,e, correspondingly.

In general, the ultrahigh EMI shielding performance of our composite aerogels is attributed to the porous microstructure and multicomponent, which leads to multiple shielding mechanisms including reflection and absorption at abundant interfaces (Figure 3g). Especially, MXene provides an efficient conductive network that enables reflection shielding at the interface. When the incident EMW reaches the surface of CMxTS$_{20}$ aerogel, part of the EMW is immediately reflected into the air, while the residual EMW entering the composite aerogel generates multiple internal reflections between MXene porous structures, leading to conductive loss to dissipate energy.[44] Additionally, rich surface terminals and local defects existing in MXene produce

dipolar polarization to improve the ultimate EMI shielding capacity. Due to the great difference in electrical conduction between TPU and MXene, the polarization phenomenon at their interface further enhances the attenuation constant. The ultrahigh EMI SE endows CM$_x$TS$_{20}$ with superior EMW shielding in real scenarios (Figure S9, Supporting Information), providing an additional way to resist a complex electromagnetic environment. The results demonstrate that the EMWs generated by electronic products can be effectively shielded by the mechanically robust and flexible CM$_x$TS$_{20}$.

As shown in Figure 1f, the EMI utilization efficiency of CM$_x$TS$_{20}$ is compared with that of MXene-based composite in previous works (see **Table 1**). Although the MXene/epoxy composite containing 4.25 wt% shows a high EMI utilization efficiency of 1082.35 dB g g^{-1},[40] but only exhibits an EMI SE of 46 dB, indicating its inadequate EMI shielding efficiency.[40] Although a high loading 70 wt% MXene leads to an ultrahigh EMI SE of 92.1 dB in the polypropylene (PP) matrix,[54] the utilization efficiency of MXene is as low as 131.57 dB g g^{-1}, which means that its manufacturing cost is very high to meet the EMI SE requirement in the industry. In comparison, our MXene aerogel shows a record-high MXene utilization efficiency of 2977.71 dB g g^{-1}, triple that of other advanced shielding materials ever reported. Moreover, the CM$_x$TS$_{20}$ achieves an

**ADVANCED
SCIENCE NEWS**

www.advancedsciencenews.com

**ADVANCED
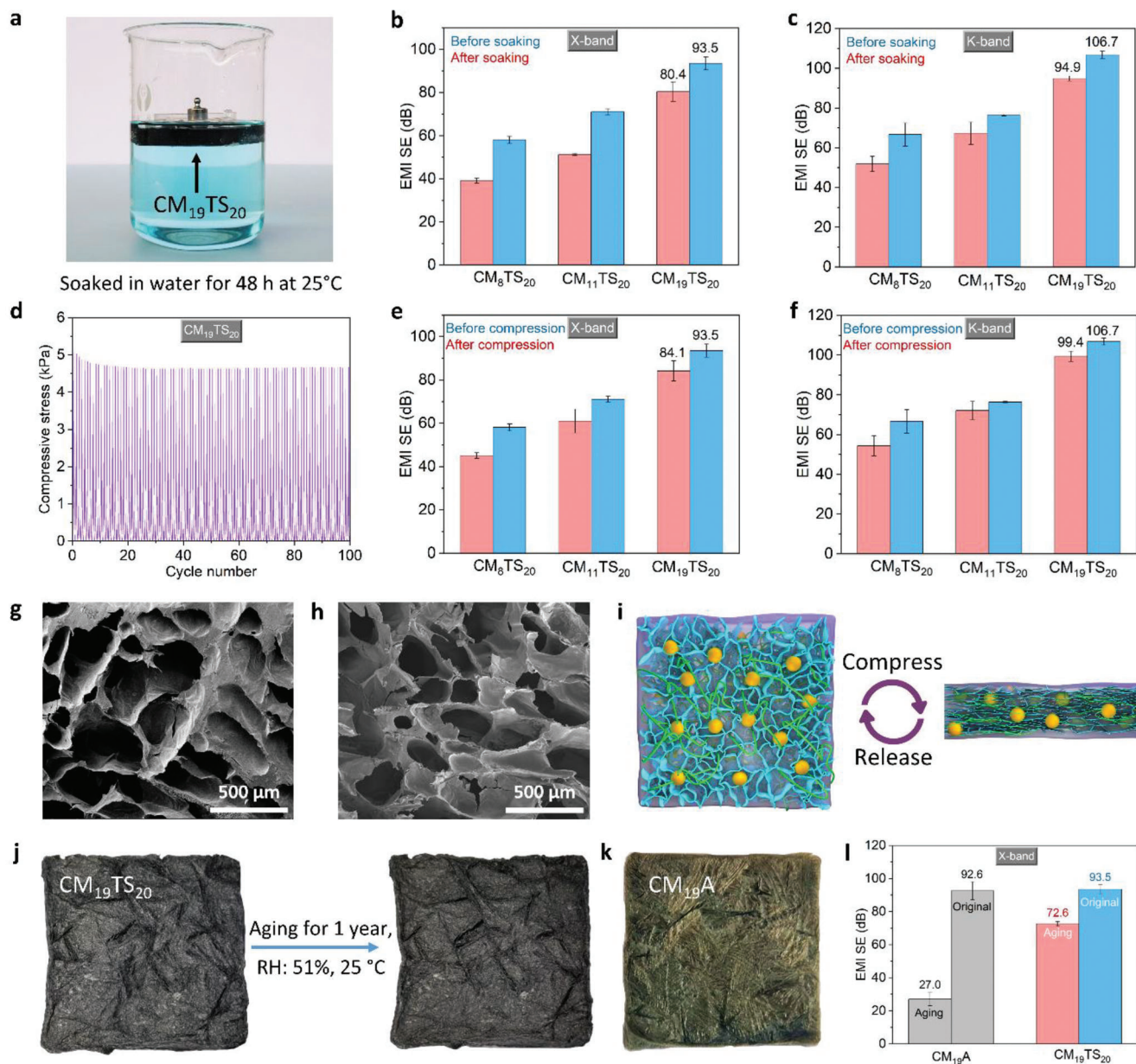FUNCTIONAL
MATERIALS**

www.afm-journal.de

Figure 4. Excellent durability and mechanical robustness. a) Digital photos of $CM_{19}TS_{20}$ immersed in water for 48 h. b) The EMI SE curves of composite aerogels before and after immersion under the X-band. c) The EMI SE histograms of composite aerogels before and after immersion under the K-band. d) Compression cycle curves of $CM_{19}TS_{20}$ under 20% strain. e) The EMI SE histograms of composite aerogels before and after compression under the X-band. f) The EMI SE histograms of composite aerogels before and after compression under the K-band. g,h) The SEM images for $CM_{19}TS_{20}$ before and after compression, respectively. i) The illustrated diagram for the compression-rebound mechanism. j) The digital photos of $CM_{19}TS_{20}$ before and after aging one year. k) Digital photo of MXene/CNF aerogel ($CM_{19}A$) without TPU protective layer after aging one year. l) The EMI SE curves of $CM_{19}TS_{20}$ MXene composite aerogel before and after aging treatment.

ultrahigh EMI SE of 93.5 dB only with an MXene loading level of 3.14 wt%. This means that a minimum loading level of MXene is required to achieve a satisfactory EMI SE, which can accelerate the practical application of expensive MXene in the industry. The water resistance of composite aerogels is critical for their practical applications. Water droplets can stay on the surface of composite aerogels without penetrating the aerogels, showing their high hydrophobic characteristic (Figure S10, Supporting Infor-

mation). Such excellent hydrophobicity enables the materials to possess a self-cleaning ability. Simply rinsing with water droplets can remove stains on the surface of the materials (Figure S11 and Movie S3, Supporting Information). After being immersed in water for 48 h, the EMI shielding performance of the CM_xTS_{20} does not decrease significantly (**Figure 4**a–c), demonstrating its excellent water resistance. The EMI SE of the $CM_{19}TS_{20}$ can reach 93.5 dB in the K-band, indicating that the composite aerogel has

**ADVANCED
SCIENCE NEWS**

www.advancedsciencenews.com

**ADVANCED
FUNCTIONAL
MATERIALS**

www.afm-journal.de

outstanding EMI shielding ability even after prolonged exposure to water. Moreover, the $CM_{19}TS_{20}$ can maintain its structural integrity without any sign of degradation or disintegration under the impact of water flow (Movie S4, Supporting Information). This observation suggests that the flame-retardant TPU provides efficient protection to the aerogel structure against water intrusion, which ensures an unchanged performance for the composite aerogels in harsh aquatic environments.

To assess the mechanical resilience of the composite aerogels, we performed compressive cycling tests on each material under a strain of 20%. The obtained results indicate that CA shows low mechanical stability with compression stress of less than 1.5 kPa due to irreversible strain upon suffering from shock (Figure S12a,b and Movie S5, Supporting Information). Notably, encapsulating with TPU or TPU/SiAPP increases the compression stress of the CA (Figure S13a–c, Supporting Information). In contrast, $CM_{19}A$ only displays maximum compressive stress of 0.75 kPa, though slight compressive resilience is observed (Figure S13d, Supporting Information). This is possibly due to its relatively loose pore structure.

Compared to those of CA, CT, CTS_{20}, or CMA, the mechanical strength and toughness of CM_xTS_{20} increase with an increment of MXene content under 100 compression cycles (Figures S13e–g, S14, and S15, Supporting Information). Particularly, the $CM_{19}TS_{20}$ exhibits prominent reversibility at a strain of 20%, with a maximum compressive stress of 4.79 kPa, five times as high as that of the MA (Figure 4d). Moreover, its maximum stress recovery ratio remains stable at ≈90.3% even after 100 compression cycles. The CM_xTS_{20} can maintain its EMI shielding performance after compression (Figure 4e,f), indicating its superiority in both mechanical resilience and EMI shielding.

The incorporation of TPU significantly contributes to the enhanced mechanical properties of the resulting composite aerogels. The surface morphologies of the TPU encapsulated composite aerogel before and after compression are shown in Figure 4g,h, respectively. The density and size of pores in the aerogel are consistent before and after compression (Figure S16a–g, Supporting Information). Furthermore, the flame-retardant TPU uniformly coats the surface and inside the void of the aerogel (Figure S16h, Supporting Information), acting as a wrapping support for enhancing the resilience of the aerogel. In contrast, the pristine CMA has wrinkles in the pores after compression (Figure S17, Supporting Information). Although the hydrogen bonds between CNF and MXene act as supporters, they are still susceptible to cracking and do not contribute to pressure resistance. Compared to the pure CA (Figure S18a–d, Supporting Information), both CT and CTS_{20} display more orderly inner pores (Figure S18e–l, Supporting Information), which can lead to better resilience performances.

Above results enable us to gain a better understanding of the mechanism governing the enhanced mechanical properties of CM_xTS_{20}. As illustrated in Figure 4i, 1D CNFs and 2D $Ti_3C_2T_x$ nanosheets form a solid aerogel skeleton through hydrogen bonding. The additional TPU encapsulation and immersion further strengthen the frameworks of these aerogels. Upon compression, the CNF-MXene skeleton wrapped by the flame-retardant TPU elastomer begins to compress. The hydrogen bonding between them and the excellent protection of the TPU elastomer can prevent the formation of

irreversible compression deformation during compression and avoid the occurrence of displacement and deformation during rebound. Overall, the synergistic effects among hydrogen bonds, flexible CNFs, anisotropic interconnection networks, and the TPU elastomer guarantee superior compression resilience of the CMA.

In addition, the TPU layer can serve as a protective coating to prevent MXene aerogels from oxidation in the air. As-prepared $CM_{19}TS_{20}$ does not show oxidation, and obvious collapse on the aerogel surface does not occur after aging for one year (Figure 4j), indicating its exceptional durability in the air. In sharp comparison, the CNF/MXene aerogel (CM19A) without TPU protection presents an apparent oxidation phenomenon after one year of aging (Figure 4k; Figure S19, Supporting Information). The EMI SE furtherly confirms the protection effect of TPU encapsulation on MXene aerogels. The $CM_{19}A$ aerogels show a substantial decrease in EMI SE from 92.6 to 27.0 dB. In contrast, the EMI SE of the $CM_{19}TS_{20}$ only reduces from 93.5 to 72.6 dB after one year (Figure 4l), clearly demonstrating that the TPU layer protects MXene from oxidation.

The practical applications of most EMI shielding composite aerogels have been often limited by their high flammability. Therefore, it is necessary to reduce their high flammability and to effectively monitor major fire risks to avoid catastrophic fire disasters. Among our as-prepared aerogels, the CM_xTS_{20} composite aerogels have the highest thermal stability with the highest char residual content, which can be attributed to the synergistic effect between SiAPP and MXene (Figure S20, Supporting Information). The alcohol lamp burning experiment reveals that CA and CT have high flammability (Figure S21a,b, Movies S6 and S7, Supporting Information) because CT has a high fire risk due to the inherent flammability of CNF and TPU. However, $CM_{19}TS_{20}$ can self-extinguish immediately upon the removal of the alcohol lamp (Figure S21c and Movie S8, Supporting Information). Moreover, the total heat release, smoke production rate, total smoke release, and carbon monoxide production rate of CM_xTS_{20} are reduced to different extents relative to those of CT (Figure S22 and Table S1, Supporting Information), indicating the high fire safety of CM_xTS_{20}.

Digital photographs (Figure S23, Supporting Information) and SEM images of the char residues (Figures S24 and S25, Supporting Information) manifest that compared with CT and CTS_{20}, CM_xTS_{20} generates a continuous dense and smooth char residue with the highest graphitization degree (Figures S26 and S27, Supporting Information), which prevents the heat transfer and the release of toxic fumes from composite aerogels. Interestingly, N and P elements are found to be mainly present in the external layer of char residue, while the Ti element predominantly occurs in the internal layer of char residue for $CM_{19}TS_{20}$, which is responsible for the formation of high-quality char layers (Figures S28–S30, Supporting Information). Upon being heated, the SiAPP will degrade to generate polyphosphoric acid which can promote the formation of a continuous and compact char layer. Meanwhile, SiAPP also thermally decomposes into phosphorus-containing radicals, such as $PO_2\bullet$, $HPO\bullet$, and $PO\bullet$, to capture the radicals produced by the chain breakage of TPU (Figure S31, Supporting Information). In brief, SiAPP and MXene work synergistically to achieve such excellent flame retardancy for CM_xTS_{20}.
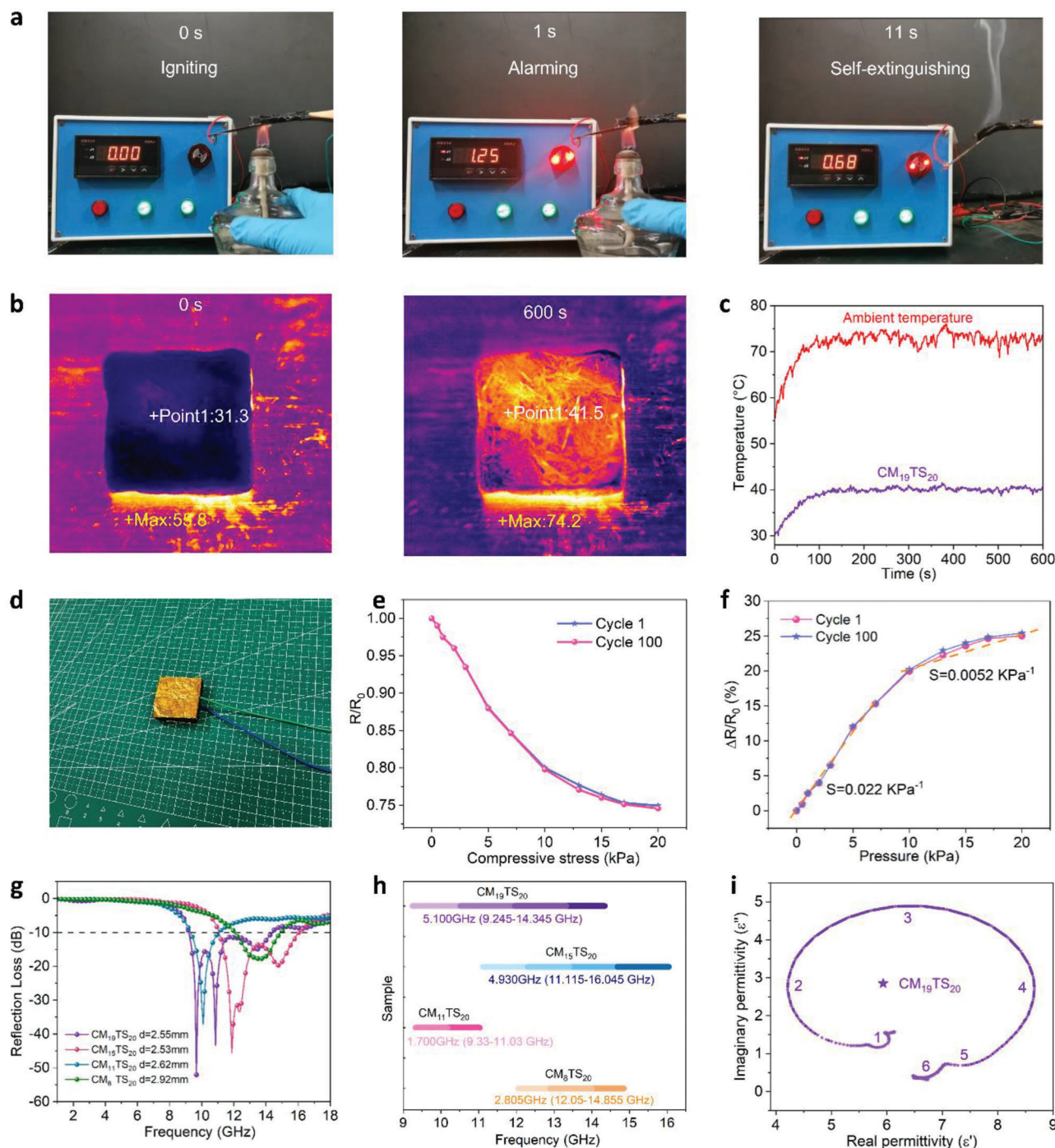
**ADVANCED
SCIENCE NEWS**

www.advancedsciencenews.com

**ADVANCED
FUNCTIONAL
MATERIALS**

www.afm-journal.de

Figure 5. Multifunctionalities of as-prepared MXene composite aerogels. a) Video snapshots of the fire-warning test, demonstrating its good fire retardancy and fire-warning capabilities. b) Thermal infrared images of $CM_{19}TS_{20}$ captured at 0 and 600 s, respectively. The temperature of the heating platform was set to 80 °C, showing its excellent thermal insulation property. c) Variation of the temperature detected on the upper surface of $CM_{19}TS_{20}$ and the heating platform. d) Schematic illustration for the fabrication of the pressure sensor. e) R/R_0 at 20% strain for 100 cycles. f) Pressure–response curves for $CM_{19}TS_{20}$. g) The reflection loss data of CM_xTS_{20} samples. h) EAB of CM_xTS_{20} in X- and Ku-band. i) The Cole–Cole semicircles of $CM_{19}TS_{20}$.

Apart from outstanding flame retardancy, the CM_xTS_{20} aerogel exhibits the ability to monitor fires at a very early stage. As shown in **Figure 5**a, the $CM_{19}TS_{20}$ can trigger the alarm within 1 s after igniting, and the fire self-extinguishes within 10 s after the alcohol lamp is removed (Movie S9, Support-

ing Information), further verifying its superior flame-retardant performance.

The aerogels often show low thermal conductivity, making them good thermal insulation materials. $CM_{19}TS_{20}$ possesses a low thermal conductivity of 0.047 W m^{-1} K^{-1}, which is only half

**ADVANCED
SCIENCE NEWS**

www.advancedsciencenews.com

**ADVANCED
FUNCTIONAL
MATERIALS**

www.afm-journal.de

of that of CA (Figure S32a, Supporting Information). To demonstrate the thermal insulation performance, as-prepared composite aerogels were placed on a heating platform with its bottom surface closely contacting the platform and heated uniformly to 80 °C (Figure S32b, Supporting Information). Based on thermal infrared images of the samples captured at 0 and 600 s (Figure 5b,c), the temperature of the $CM_{19}TS_{20}$ is ≈32.7 °C lower than the ambient temperature (80 °C) after 600 s of heating, demonstrating its excellent thermal insulation ability.

Compressible and elastic carbon aerogels have been widely investigated for their potential application in wearable pressure- or strain-sensing electronics and electronic skins due to their chemical and thermal stability, excellent conductivity, and shape memory.[56] As-developed $CM_{19}TS_{20}$ was utilized as a pressure-sensing material by sandwiching it between two copper electrodes (Figure 5d). The electronic resistance was recorded as the surface pressure of the copper electrode was changed. The normalized electrical resistance (R/R_0) of the $CM_{19}TS_{20}$ exhibits a linear decrease at stresses below 10 kPa (Figure 5e), suggesting a rapid increase in contact area among carbon lamellae. Moreover, the R/R_0 curve maintains a consistent shape even after 100 cycles, indicating highly stable conductivity during cyclic compression. The flexible and elastic carbon layers in $CM_{19}TS_{20}$ are responsible for the excellent stability of the R/R_0 curve. The electronic resistance variation ratios ($\Delta R/R_0 = (R_0-R_P)/R_0$, where R_0 and R_P denote the resistance without and with applied pressure, respectively) were calculated based on measured values and plotted as a function of applied pressure (P) and shown in Figure 5f. The pressure sensitivity (S) was defined as the slope of the curves ($S = \delta(\Delta R/R_0)/\delta P$.[57] The low-pressure regime from 0 to 7.0 kPa exhibits a linearly increasing slope with a sensitivity of 0.022 kPa^{-1}. In the large-pressure regime (10.0–20.0 kPa), the sensitivity of the $CM_{19}TS_{20}$ is 0.052 kPa^{-1}. These results demonstrate that the $CM_{19}TS_{20}$ has excellent pressure sensitivity, making it a promising candidate for the manufacture of low-cost wearable materials, artificial skin, and sensors.

As depicted in Figure 5g, our composite aerogels possess excellent EMW absorption performance, as evidenced by their strong absorption capabilities in frequency bands ranging from the X-band to the Ku-band. The $CM_{15}TS_{20}$ shows a robust absorption performance of −45.55 dB at 11.88 GHz, while the $CM_{11}TS_{20}$ exhibits an RL$_{min}$ of −37.07 dB at 10.09 GHz. Similarly, the CM_9TS_{20} displays an RL$_{min}$ of −17.81 dB at 13.58 GHz (Figure S33, Supporting Information). The $CM_{19}TS_{20}$ presents strong absorption of 52.06 dB at 9.67 GHz and remarkable broadband absorption capabilities. Impressively, the largest effective absorption bandwidth of 5.10 GHz (9.2445–13.345 GHz) can be obtained at a matching thickness of 2.55 mm for $CM_{19}TS2_0$ instead of $CM_{15}TS_{20}$ (4.93 GHz), $CM_{11}TS_{20}$ (1.70 GHz), and CM_8TS_{20} (2.80 GHz) (Figure 5h). Figure 5i depicts the Cole–Cole plots of the $CM_{19}TS_{20}$, showing a response behavior of dielectric loss, where each semicircle corresponds to a Debye polarization relaxation. The $CM_{19}TS_{20}$ exhibits several obvious semicircles, suggesting that its relaxation process can be attributed to residual defects in MXene, dipole polarization generated by residual oxygen-containing groups, polarization generated by delocalized electrons, interface polarization at the interface between MXene and CNF, and interface polarization at the interface of MXene nanoparticles themselves. A similar phenomenon can be observed in other CM_xTS_{20} composite aerogels (Figure S34, Supporting Information). These findings clarify the diverse mechanisms underlying the exceptional EMI shielding properties of $CM_{19}TS_{20}$, opening a promising route for the design of advanced EMI shielding materials.

3. Conclusion

We develop a novel approach for fabricating a series of lightweight, flexible, and hydrophobic MXene composite aerogels with superior EMI-shielding, mechanical ultra-elasticity and robustness, flame retardancy, heat insulation, and weather resistance. The CNF-MXene aerogel is successfully encapsulated by flame retardant TPU, resulting in extraordinary water tolerance, outstanding durability, and high flexibility for the composite aerogels. Furthermore, the favorable porous structures not only greatly improve the EMI performance to 93.5 dB, but also lead to an ultra-high utilization efficiency of MXene up to 2977.71 dB g g^{-1} by providing more multiple interfaces to attenuate the EMWs. Our mechanically hyperelastic, robust, durable, and multifunctional MXene composite aerogels with remarkable EMI shielding performance show great potential in defense, aerospace, and smart wearable electronics.

4. Experimental Section

Raw Materials: Cellulose nanofibers (CNF) aqueous solution (1 wt%) purchased from Guilin Qihong Technology Co., Ltd., had a diameter of 4−10 nm and a length of 1−3 μm. The Ti_3AlC_2 powders with a size of 400 mesh (99%) were obtained from 11 Technology Co., Ltd. (Changchun, China). Lithium fluoride (LiF, 98.5%) and hydrochloric acid (HCl, 36.5%) were afforded by the Sinopharm Chemical Reagent Co., Ltd. (Shanghai, China). Thermoplastic polyurethane elastomer (TPU, 65E85) was produced by Bangtai Chemical Industry Co., Ltd. (Baoding, China). Silicon microencapsulated ammonium polyphosphate (SiAPP) (203) was bought from Sichuan Refining Chemical Co., Ltd., (Chengdu, China), which was synthesized by mixing ammonium polyphosphate, tetraethoxysilane (TEOS), alkylphenol polyoxyethylene (APEO), and ammonia in solution. N, N-Dimethylformamide (DMF, analytical reagent (AR)) was obtained from Aladdin Reagent Co., Ltd., (Shanghai, China).

Synthesis of CNF-$Ti_3C_2T_x$ Hybrid Aerogel: $Ti_3C_2T_x$ MXene nanosheets were prepared from Ti_3AlC_2 according to the modified HF etching method.[58] A facile fabrication process of the hybrid aerogels was introduced in this paper. Firstly, the MXene aqueous solution (8, 11, and 19 mg g^{-1}) was added into a three-necked flask and stirred under ultrasonic conditions for 30 min under the glaciofluvial condition. After that, CNF aqueous solution (10 mg mL^{-1}) was dropped into the solution under sonication and stirred for 2 h to obtain a homogenous CNF-MXene solution. Then, the CNF-MXene solution was frozen at −25 °C for 48 h and lyophilized in a freeze dryer under −50 °C for 48 h to obtain CNF-MXene aerogel (CMA). As a comparison, pure MXene aerogel (MA) was also prepared.

Fabrication of Encapsulated CNF-MXene Composite Aerogels: To prepare composite aerogels with better mechanical properties, excellent flame retardancy, and weather resistance, CMA was subsequently encapsulated with TPU/SiAPP solution to environmental stability and service life of the multifunctional aerogel by preventing the oxidation and degradation of its MXene component. The mixture of 48.0 g TPU, and 480 mL DMF was stirred uniformly and transparently at 80 °C for 2 h. Afterward, 12.0 g SiAPP was added to the solution and mechanically stirred for 30 min. Then, the aerogels were immersed in the mixture for 90 s. Finally, the encapsulated aerogels were dried under vacuum at 80 °C for 48 h. To facilitate the following discussion, the materials were named, such as CM_8TS_{20}, where

**ADVANCED
SCIENCE NEWS**

www.advancedsciencenews.com

**ADVANCED
FUNCTIONAL
MATERIALS**

www.afm-journal.de

C, M, and T represented CNF, MXene, and TPU, respectively, and the suffixes 8 and 20 respectively represented the MXene concentration of 8 mg g^{-1} and the mass fraction of SiAPP in TPU. As a comparison, pure CNF aerogel (CA) encapsulated with TPU or TPU/SiAPP was also prepared.

Characterization: The electromagnetic-field intensity of the environment was measured with an electromagnetic-field tester (LZT-1000, Long Zhentian (Beijing) Electronic Instrument Co., Ltd.). Scanning electron microscopy (SEM, FEI Nova NanoSEM230, USA) was used to observe the surface morphologies of the composite aerogels and their char residues. X-ray diffraction (XRD) patterns were obtained by DY1602/Empyrean X-ray diffractometer (Panalytical, Netherlands) equipped with Cu Kα radiation (λ = 1.54178 Å). Fourier transform infrared (FTIR) spectra were estimated by Nicolet IS50 spectrometer (Nicolet Instrument Company, USA). The scanning range was in the wavenumber of 4000–400 cm^{-1}.

Thermogravimetric analysis (TGA) of the flame retardant and composite aerogels was investigated using an automatic sampling synchronous thermal analyzer (STA449F5) from 30 to 800 °C with a ramp rate of 20 °C min^{-1} in an argon atmosphere. The combustion property of composite aerogels was investigated by a TTech-GBT16172-2 type cone calorimetry (TESTech, Suzhou, China) with a dimension of 100.0 × 100.0 × 10.0 mm^3 according to the ISO 5660 standard under a heat flux of 35 kW m^{-2}. Raman spectroscopy was measured on a Raman microscope (InviaReflex, Renishaw Invia, UK) in a wavenumber range of 200–2000 cm^{-1}, and the excitation wavelength was 532 nm. X-ray photoelectron spectrum (XPS) was measured using a Thermo Fisher Scientific K-Alpha spectrometer (Waltham, USA). The excitation source was an Al Kα ray at 1253.6 eV. Transmission electron microscope (TEM) images were collected by a TECNAI G2 F20 instrument with an accelerating voltage of 200 kV (FEI Co., USA). The thickness of exfoliated Ti$_3$C$_2$T$_x$ was measured by atomic force microscopy (AFM, Veeco DI Multimode V, USA) in a scanning mode.

Temperature sensing and fire warning tests were demonstrated by connecting CM$_{19}$TS$_{20}$ (100 mm × 20 mm × 8 mm) with a digital multimeter (DMM6500 6 1/2, Keithley Instrument, US), an alarm device, and a hot plate flame in series through the wire. An alcohol lamp flame with a length of 40 mm was used for the fire-warning test. The triggered time versus the output voltage curve was recorded. The electrical resistance of the CM$_{19}$TS$_{20}$ was measured using a digital multimeter (Keysight, 34465A, USA) connected to the computer. The top and bottom surfaces of CM$_{19}$TS$_{20}$ cylinders were glued to copper foils with conductive silver paint, and the copper foils were connected to the multimeter using copper wires for electric resistance measurement. The electromagnetic parameters in the frequency of 2–18 GHz were obtained by a vector network analyzer (Agilent HP-8722ES) using the coaxial-line method. The samples were machined to a toroidal shape of 7.0 mm in outer diameter, 3.04 mm in inner diameter, and a thickness of ≈3.5 mm for the characterization.

The specimens for compression testing were prepared according to ASTM D695. The specimens were fabricated as blocks of 60 mm × 60 mm × 10 mm. The compression testing was carried out by Instron 3366 testing machine with a load capacity of 10 kN at a constant compression rate of 2 mm min^{-1}. The EMI SE of the CM$_x$TS$_{20}$ composite aerogels in the X-band range (8.2–12.4 GHz) and K-band range (18.0–26.5 GHz), and their S-parameters (S_{11} and S_{21}) were measured by waveguide method (Vector Network Analyzer N5222B) according to ASTM D4935-2010. According to Schelkunoff's theory, total EMI SE (SE$_T$) is composed of reflection (SE$_R$) and absorption (SE$_A$).[1a] The detailed calculation follows Equations (1–4).

$$R = |S_{11}|^2, \ T = |S_{21}|^2 \tag{1}$$

$$1 = A + R + T \tag{2}$$

$$SE_R = -10 \log |1 - R|, \ SE_A = -10 \log |T/(1-R)| \tag{3}$$

$$SE_T = SE_R + SE_A = -10 \log T \tag{4}$$

where R, A, and T mean reflection, absorption, and transmission coefficients, respectively.

Supporting Information

Supporting Information is available from the Wiley Online Library or from the author.

Conflict of Interest

The authors declare no conflict of interest.

Data Availability Statement

The data that support the findings of this study are available from the corresponding author upon reasonable request.

[1] a) J. Jing, Z. Ma, R. Jiang, Y. Zhang, L. Shao, *Adv. Eng. Mater.* **2023**, *25*, 2201938; b) C. Wei, Q. Zhang, Z. Wang, W. Yang, H. Lu, Z. Huang, W. Yang, J. Zhu, *Adv. Funct. Mater.* **2023**, *33*, 2211889.

[2] a) Y. Shi, A. Yao, J. Han, H. Wang, Y. Feng, L. Fu, F. Yang, P. Song, *J. Colloid. Interface Sci.* **2023**, *640*, 179; b) L. Liu, Z. Ma, M. Zhu, L. Liu, J. Dai, Y. Shi, J. Gao, T. Dinh, T. Nguyen, L.-C. Tang, *J. Mater. Sci. Technol.* **2023**, *132*, 59.

[3] a) L. Liu, J. Feng, Y. Xue, V. Chevali, Y. Zhang, Y. Shi, L. C. Tang, P. Song, *Adv. Funct. Mater.* **2023**, *33*, 2212124; b) K. Chen, Y. Feng, Y. Shi, H. Wang, L. Fu, M. Liu, Y. Lv, F. Yang, B. Yu, M. Liu, *Compos. Pt. A-Appl. Sci. Manuf.* **2022**, *160*, 107070.

[4] Y. Feng, H. Liu, W. Zhu, L. Guan, X. Yang, A. V. Zvyagin, Y. Zhao, C. Shen, B. Yang, Q. Lin, *Adv. Funct. Mater.* **2021**, *31*, 2105264.

[5] T. Kshetri, D. T. Tran, H. T. Le, D. C. Nguyen, H. Van Hoa, N. H. Kim, J. H. Lee, *Prog. Mater. Sci.* **2021**, *117*, 100733.

[6] M. Han, X. Yin, K. Hantanasirisakul, X. Li, A. Iqbal, C. B. Hatter, B. Anasori, C. M. Koo, T. Torita, Y. Soda, *Adv. Opt. Mater.* **2019**, *7*, 1900267.

[7] R. Bian, G. He, W. Zhi, S. Xiang, T. Wang, D. Cai, *J. Mater. Chem. C* **2019**, *7*, 474.

[8]   S. Zhao, H.-B. Zhang, J.-Q. Luo, Q.-W. Wang, B. Xu, S. Hong, Z.-Z. Yu, *ACS Nano* **2018**, *12*, 11193.

[9]   C. Liang, H. Qiu, P. Song, X. Shi, J. Kong, J. Gu, U.-l. M. Aerogel, *Sci. Bull.* **2020**, *65*, 616.

[10] P. Sambyal, A. Iqbal, J. Hong, H. Kim, M.-K. Kim, S. M. Hong, M. Han, Y. Gogotsi, C. M. Koo, *ACS Appl. Mater. Interfaces* **2019**, *11*, 38046.

[11] H. Liu, X. Chen, Y. Zheng, D. Zhang, Y. Zhao, C. Wang, C. Pan, C. Liu, C. Shen, *Adv. Funct. Mater.* **2021**, *31*, 2008006.

[12] P. Lin, J. Xie, Y. He, X. Lu, W. Li, J. Fang, S. Yan, L. Zhang, X. Sheng, Y. Chen, *Sol. Energy Mat. Sol. C* **2020**, *206*, 110229.

[13] H. Gao, N. Bing, Z. Bao, H. Xie, W. Yu, *Chem. Eng. J.* **2023**, *454*, 140362.

[14] J. Zhou, M. Xie, F. Wu, Y. Mei, Y. Hao, L. Li, R. Chen, *Adv. Mater.* **2022**, *34*, 2106897.

[15] N. Wu, Y. Yang, C. Wang, Q. Wu, F. Pan, R. Zhang, J. Liu, Z. Zeng, *Adv. Mater.* **2023**, *35*, 2207969.

[16] a) T. Gao, Y. Ma, L. Ji, Y. Zheng, S. Yan, Y. Li, X. Zhang, *Adv. Compos. Hybrid. Ma.* **2022**, *5*, 2328; b) A. Pasha, S. Khasim, S. Manjunatha, *J. Mater. Sci-Mater. El.* **2023**, *34*, 409; c) A. U. Rehman, M. Atif, U. u. Rehman, H. Wahab, F. C.-C. Ling, W. Khalid, A. Ul-Hamid, Z. Ali, M. Nadeem, *Mater. Today Commun.* **2023**, *34*, 105454.

[17] Y. Wang, Q. Qi, G. Yin, W. Wang, D. Yu, *ACS Appl. Mater. Interfaces* **2021**, *13*, 21831.

[18] H. Liu, Z. Huang, T. Chen, X. Su, Y. Liu, R. Fu, *Chem. Eng. J.* **2022**, *427*, 131540.

[19] G.-Y. Yang, S.-Z. Wang, H.-T. Sun, X.-M. Yao, C.-B. Li, Y.-J. Li, J.-J. Jiang, *ACS Appl. Mater. Interfaces* **2021**, *13*, 57521.

[20] Z. Zong, P. Ren, Z. Guo, J. Wang, Z. Chen, Y. Jin, F. Ren, *J. Colloid. Interface Sci.* **2022**, *619*, 96.

[21] Y. Yang, N. Wu, B. Li, W. Liu, F. Pan, Z. Zeng, J. Liu, *ACS Nano* **2022**, *16*, 15042.

[22] H. Xu, X. Yin, X. Li, M. Li, S. Liang, L. Zhang, L. Cheng, *ACS Appl. Mater. Interfaces* **2019**, *11*, 10198.

[23] X. Du, J. Wang, L. Jin, S. Deng, Y. Dong, S. Lin, *ACS Appl. Mater. Interfaces* **2022**, *14*, 15225.

[24] a) Y. Zhu, J. Liu, T. Guo, J. J. Wang, X. Tang, V. Nicolosi, *ACS Nano* **2021**, *15*, 1465; b) G. M. Weng, J. Li, M. Alhabeb, C. Karpovich, H. Wang, J. Lipton, K. Maleski, J. Kong, E. Shaulsky, M. Elimelech, *Adv. Funct. Mater.* **2018**, *28*, 1803360.

[25] A. Iqbal, F. Shahzad, K. Hantanasirisakul, M.-K. Kim, J. Kwon, J. Hong, H. Kim, D. Kim, Y. Gogotsi, C. M. Koo, *Science* **2020**, *369*, 446.

[26] A. Iqbal, J. Hong, T. Y. Ko, C. M. Koo, *Nano Converg.* **2021**, *8*, 9.

[27] C. J. Zhang, S. Pinilla, N. McEvoy, C. P. Cullen, B. Anasori, E. Long, S.-H. Park, A. Seral-Ascaso, A. Shmeliov, D. Krishnan, *Chem. Mater.* **2017**, *29*, 4848.

[28] S. Huang, V. N. Mochalin, *Inorg. Chem.* **2019**, *58*, 1958.

[29] X. Zhao, A. Vashisth, E. Prehn, W. Sun, S. A. Shah, T. Habib, Y. Chen, Z. Tan, J. L. Lutkenhaus, M. Radovic, *Matter* **2019**, *1*, 513.

[30] H. Wang, J. Wang, Y. Shi, L. Fu, M. Liu, Y. Feng, B. Yu, J. Gao, F. Yang, *Compos. Commun.* **2022**, *34*, 101270.

[31] a) M. Alhabeb, K. Maleski, B. Anasori, P. Lelyukh, L. Clark, S. Sin, Y. Gogotsi, *Chem. Mater.* **2017**, *29*, 7633; b) X. Li, X. Yin, C. Song, M. Han, H. Xu, W. Duan, L. Cheng, L. Zhang, *Adv. Funct. Mater.* **2018**, *28*, 1803938.

[32] H. Qin, Y. Zhang, J. Jiang, L. Wang, M. Song, R. Bi, P. Zhu, F. Jiang, *Adv. Funct. Mater.* **2021**, *31*, 2106269.

[33] W. Tian, A. VahidMohammadi, M. S. Reid, Z. Wang, L. Ouyang, J. Erlandsson, T. Pettersson, L. Wågberg, M. Beidaghi, M. M. Hamedi, *Adv. Mater.* **2019**, *31*, 1902977.

[34] S. Wan, X. Li, Y. Wang, Y. Chen, X. Xie, R. Yang, A. P. Tomsia, L. Jiang, Q. Cheng, *Proc. Natl. Acad. Sci. U. S. A.* **2020**, *117*, 27154.

[35] X. Ma, J. Pan, H. Guo, J. Wang, C. Zhang, J. Han, Z. Lou, C. Ma, S. Jiang, K. Zhang, *Adv. Funct. Mater.* **2023**, *33*, 2213431.

[36] a) X. Guan, Z. Yang, M. Zhou, L. Yang, R. Peymanfar, B. Aslibeiki, G. Ji, *Small Struct.* **2022**, *3*, 2200102; b) M.-S. Cao, Y.-Z. Cai, P. He, J.-C. Shu, W.-Q. Cao, J. Yuan, *Chem. Eng. J.* **2019**, *359*, 1265.

[37] R. Sun, H. B. Zhang, J. Liu, X. Xie, R. Yang, Y. Li, S. Hong, Z. Z. Yu, *Adv. Funct. Mater.* **2017**, *27*, 1702807.

[38] Y. Du, J. Xu, J. Fang, Y. Zhang, X. Liu, P. Zuo, Q. Zhuang, *J. Mater. Chem. A* **2022**, *10*, 6690.

[39] X. Wu, B. Han, H.-B. Zhang, X. Xie, T. Tu, Y. Zhang, Y. Dai, R. Yang, Z.-Z. Yu, *Chem. Eng. J.* **2020**, *381*, 122622.

[40] L. Wang, H. Qiu, P. Song, Y. Zhang, Y. Lu, C. Liang, J. Kong, L. Chen, J. Gu, *Compos. Pt. A-Appl. Sci. Manuf.* **2019**, *123*, 293.

[41] Y. Zhang, J. Yu, J. Lu, C. Zhu, D. Qi, *J. Alloy. Compd.* **2021**, *870*, 159442.

[42] Z. Lu, F. Jia, L. Zhuo, D. Ning, K. Gao, F. Xie, *Compos. Part B-Eng.* **2021**, *217*, 108853.

[43] F. Shahzad, M. Alhabeb, C. B. Hatter, B. Anasori, S. Man Hong, C. M. Koo, Y. Gogotsi, *Science* **2016**, *353*, 1137.

[44] J. Liu, H. B. Zhang, R. Sun, Y. Liu, Z. Liu, A. Zhou, Z. Z. Yu, *Adv. Mater.* **2017**, *29*, 1702367.

[45] M. Han, C. E. Shuck, R. Rakhmanov, D. Parchment, B. Anasori, C. M. Koo, G. Friedman, Y. Gogotsi, *ACS Nano* **2020**, *14*, 5008.

[46] P. He, M.-S. Cao, Y.-Z. Cai, J.-C. Shu, W.-Q. Cao, J. Yuan, *Carbon* **2020**, *157*, 80.

[47] C. Lei, Y. Zhang, D. Liu, K. Wu, Q. Fu, *ACS Appl. Mater. Interfaces* **2020**, *12*, 26485.

[48] F. Xie, F. Jia, L. Zhuo, Z. Lu, L. Si, J. Huang, M. Zhang, Q. Ma, *Nanoscale* **2019**, *11*, 23382.

[49] Z. Ma, S. Kang, J. Ma, L. Shao, Y. Zhang, C. Liu, A. Wei, X. Xiang, L. Wei, J. Gu, *ACS Nano* **2020**, *14*, 8368.

[50] S. J. Wang, D. S. Li, L. Jiang, *Adv. Mater. Interfaces* **2019**, *6*, 1900961.

[51] F. Qi, L. Wang, Y. Zhang, Z. Ma, H. Qiu, J. Gu, *Mat. Today Phys.* **2021**, *21*, 100512.

[52] E. Kim, H. Zhang, J.-H. Lee, H. Chen, H. Zhang, M. H. Javed, X. Shen, J.-K. Kim, *Compos. Pt. A-Appl. Sci. Manuf.* **2021**, *147*, 106430.

[53] T. Tang, S. Wang, Y. Jiang, Z. Xu, Y. Chen, T. Peng, F. Khan, J. Feng, P. Song, Y. Zhao, *J. Mater. Sci. Technol.* **2022**, *111*, 66.

[54] X. Zheng, J. Tang, P. Wang, Z. Wang, L. Zou, C. Li, *J. Colloid. Interface Sci.* **2022**, *628*, 994.

[55] L. Jin, P. Wang, W. Cao, N. Song, P. Ding, *ACS Appl. Mater. Interfaces* **2021**, *14*, 1747.

[56] E. Roh, H. B. Lee, D. I. Kim, N. E. Lee, *Adv. Mater.* **2017**, *29*, 1703004.

[57] H. B. Yao, J. Ge, C. F. Wang, X. Wang, W. Hu, Z. J. Zheng, Y. Ni, S. H. Yu, *Adv. Mater.* **2013**, *25*, 6692.

[58] S. Gong, X. Sheng, X. Li, M. Sheng, H. Wu, X. Lu, J. Qu, *Adv. Funct. Mater.* **2022**, *32*, 2200570.